

LISICON-Based Amorphous Oxide for Bulk-Type All-Solid-State Lithium-Ion Battery

Toyoki Okumura,^{*,†} Sou Taminato,^{†,§} Yoshinobu Miyazaki,[‡] Michinori Kitamura,[‡] Tomohiro Saito,[‡] Tomonari Takeuchi,[†] and Hironori Kobayashi[†]

[†] Research Institute of Electrochemical Energy, National Institute of Advanced Industrial Science and Technology (AIST), 1-8-31 Midorigaoka, Ikeda, Osaka 563-8577, Japan

[‡] Tsukuba Laboratory, Technical Solution Headquarters, Sumika Chemical Analysis Service (SCAS), Ltd., 6 Kitahara, Tsukuba, Ibaraki 300-3266, Japan

[§] Department of Chemistry, Mie University, 1577 Kurimamachiya-cho, Tsu, Mie 514-8507, Japan

KEYWORDS: all-solid-state Li-ion battery, LISICON, solid-state electrolyte, spark-plasma sintering, low-temperature densification

*E-mail: toyoki-okumura@aist.go.jp

Phenomena under ball-milling

The solo-LGPO powder ($x = 0$) likely adhered to the bottom corners of the ZrO_2 pot after treatment. Therefore, the long-period arrangement of the crystalline LGPO was difficult to break, even though the adhered powder was raked out several times during the treatment. On the other hand, the LGPO- Li_3BO_3 blended powder was more likely to adhere to the surfaces of the ZrO_2 balls than to the walls of the ZrO_2 pot, resulting in a thicker covering of the balls with increased Li_3BO_3 additive ratio. Thus, the amorphization of LGPO- Li_3BO_3 was promoted by introducing an effective impact via ZrO_2 balls to the covered powder. Actually, slight peaks remained in the treated LGPO with a low Li_3BO_3 additive amount ($x = 1/7$) associated with the increase in bottom-corner adhesion. On the other hand, crystalline peaks were also confirmed from solo- Li_3BO_3 ($x = 1$) in spite of the effective treatment achieved by the Li_3BO_3 -covered balls [Figure 1(h)]. These peaks indicate that the compositional combination of LGPO and Li_3BO_3 , in addition to the ball-adhering effect by Li_3BO_3 additive, was also important for amorphization.

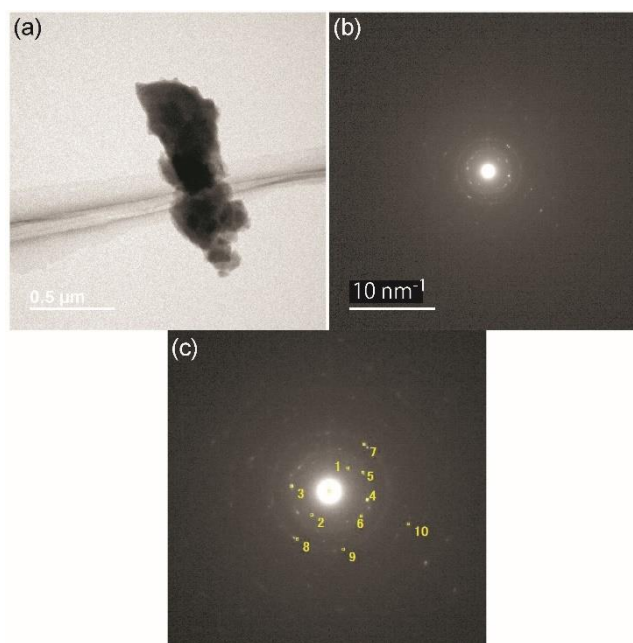


Figure S1. (a) Bright-field TEM image and (b) selected-area electron diffraction of crystalline LGPO electrolyte. (c) Selected diffraction spots for estimating the reflection planes of LGPO.

Table S1. Reflection planes of LGPO corresponding to selected diffraction spots in Figure S1(c).

Spot number	d^* / nm^{-1}	Amplitude	Reflection plane candidate of $\text{Li}_{3.75}\text{Ge}_{0.75}\text{P}_{0.25}\text{O}_4$
#1	1.88	1377	2 0 0
#2	1.86	1311	2 0 0
#3	2.40	2430	2 1 0
#4	2.50	3645	2 1 0 or 0 1 1
#5	2.46	1680	2 1 0 or 0 1 1
#6	2.59	1380	0 1 1 or 2 0 1
#7	3.71	2522	2 2 0, 4 0 0, or 3 1 1
#8	3.66	1299	2 2 0, 4 0 0, or 3 1 1
#9	3.80	740	2 2 0, 4 0 0, or 3 1 1
#10	5.46	1037	4 0 2 or 2 2 2

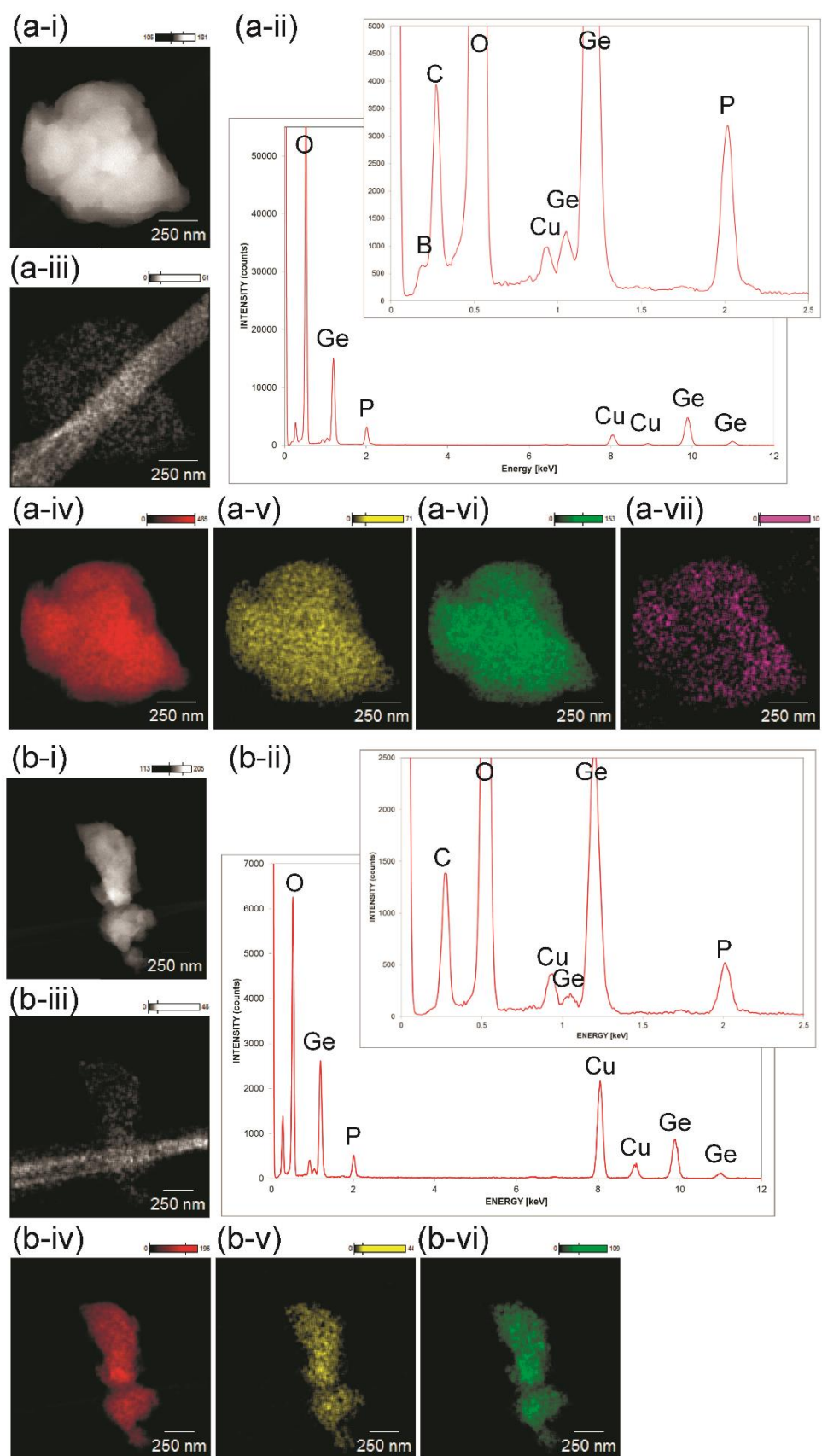


Figure S2. STEM-EDS results of (a) amorphous 0.5LGPO-0.5Li₃BO₃ and (b) LGPO; (i) STEM image, (ii) EDS spectrum, and STEM-EDS mappings of (iii) C, (iv) O, (v) P, (vi) Ge, and (vii) B.

Wide amorphization permissibility of LISICON-based oxides

The amorphization of LISICON-based oxides was attempted with other LISICON-borate additive combinations, whose powder XRD patterns are shown in Figure S3. Amorphous halo patterns were confirmed in all of the LISICON- Li_3BO_3 samples in the present study with crystalline LISICON phases of $\gamma\text{-Li}_3\text{PO}_4$ -type $\text{Li}_{3.5}\text{Ge}_{0.5}\text{V}_{0.5}\text{O}_4$, $\gamma\text{-Li}_3\text{PO}_4$ -type $\text{Li}_{3.5}\text{Ge}_{0.75}\text{S}_{0.25}\text{O}_4$, and Li_4SiO_4 -type $\text{Li}_{3.625}\text{Si}_{0.375}\text{Al}_{0.125}\text{P}_{0.5}\text{O}_4$ [Figure S3(a-c)]. (Li_4SiO_4 -type ionic conductors have sometimes been included in the LISICON family.) Moreover, a similar LISICON-based amorphous phase could also be prepared from other borate additives such as $\text{Li}_4\text{B}_2\text{O}_5$, LiBO_2 , and B_2O_3 [Figure S3(d-f)] in spite of their structural differences, resulting in different chain-network structures consisting of BO_3^{3-} triangles and BO_4^{5-} tetrahedrons. Therefore, LISICON-based amorphous materials could also be prepared with various borate additives. We also attempted to prepare amorphous electrolytes with other electrolyte candidates (NASICON-type, perovskite-type, and garnet-type oxides) and other Li-salt additives (Li_2CO_3 , $\text{Li}_{2.2}\text{C}_{0.8}\text{B}_{0.2}\text{O}_3$, and LiNO_3), whose powder XRD patterns and conductivities are shown in Figure S4 and Table S2, respectively. In most cases, crystalline phases remained in other electrolyte-additive combinations after the ball-milling treatment, while some advantages were confirmed from carbonate additives. Although a NASICON-type electrolyte was also suitable for preparing the amorphous electrolyte by ball-milling with a borate additive, the conductivity was quite low at $3.2 \times 10^{-8} \text{ S cm}^{-1}$.

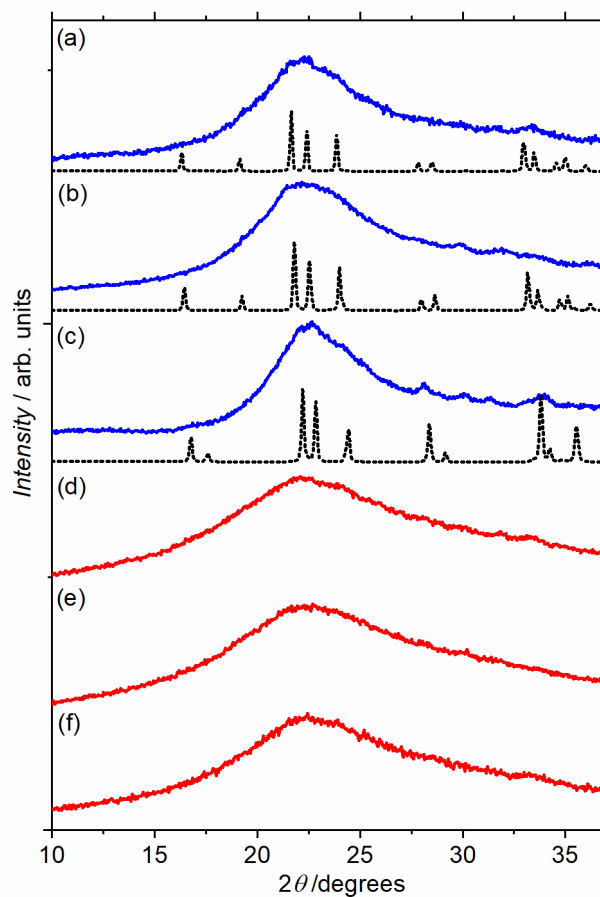


Figure S3. Powder XRD patterns of (a) $0.5\text{Li}_{3.5}\text{Ge}_{0.5}\text{V}_{0.5}\text{O}_4\text{-}0.5\text{Li}_3\text{BO}_3$, (b) $0.5\text{Li}_{3.5}\text{Ge}_{0.75}\text{S}_{0.25}\text{O}_4\text{-}0.5\text{Li}_3\text{BO}_3$, (c) $0.5\text{Li}_{3.625}\text{Si}_{0.375}\text{Al}_{0.125}\text{P}_{0.5}\text{O}_4\text{-}0.5\text{Li}_3\text{BO}_3$, (d) $0.5\text{Li}_{3.5}\text{Ge}_{0.5}\text{P}_{0.5}\text{O}_4\text{-}0.25\text{Li}_4\text{B}_2\text{O}_5$, (e) $0.5\text{Li}_{3.5}\text{Ge}_{0.5}\text{P}_{0.5}\text{O}_4\text{-}0.5\text{LiBO}_2$, and (f) $0.5\text{Li}_{3.5}\text{Ge}_{0.5}\text{P}_{0.5}\text{O}_4\text{-}0.25\text{B}_2\text{O}_3$ after ball-milling treatment. The patterns of crystalline (a) $\text{Li}_{3.5}\text{Ge}_{0.5}\text{V}_{0.5}\text{O}_4$, (b) $\text{Li}_{3.5}\text{Ge}_{0.75}\text{S}_{0.25}\text{O}_4$, and (c) $\text{Li}_{3.625}\text{Si}_{0.375}\text{Al}_{0.125}\text{P}_{0.5}\text{O}_4$ are also shown as dashed lines.

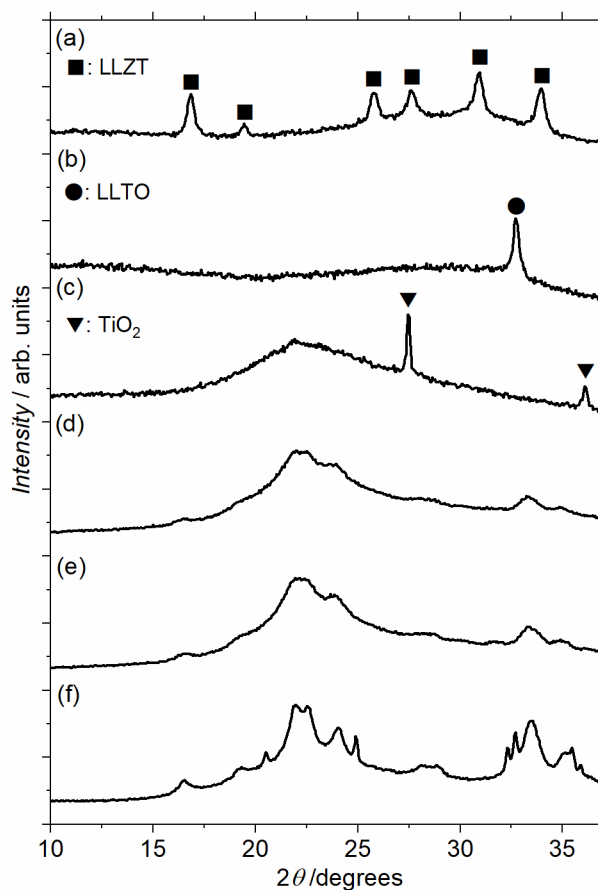


Figure S4. Powder XRD patterns of (a) 0.25[garnet-type $\text{Li}_{6.5}\text{La}_3\text{Zr}_{1.5}\text{Ta}_{0.5}\text{O}_{12}$ (LLZT)]-0.75 Li_3BO_3 , (b) 0.5[perovskite-type $\text{Li}_{0.33}\text{La}_{0.56}\text{TiO}_3$ (LLTO)]-0.5 Li_3BO_3 , (c) 0.25[NASICON-type Al-doped $\text{LiTi}_2(\text{PO}_4)_3$]-0.75 Li_3BO_3 , (d) 0.5LGPO-0.5 Li_2CO_3 , (e) 0.5LGPO-0.5 $\text{Li}_{2.2}\text{C}_{0.8}\text{B}_{0.2}\text{O}_3$, and (f) 0.5LGPO-0.5 LiNO_3 after ball-milling treatment.

Table S2. Conductivities at 25 °C for various Li-ion conductive oxide-additive blended electrolytes by ball-milling treatment.

Li-ion conductive oxide	Additive	Blending molar ratio	Conductivity at 25 °C / S cm ⁻¹
$\text{Li}_{3.75}\text{Ge}_{0.75}\text{P}_{0.25}\text{O}_4$	Li_3BO_3	1 : 1	1.5×10^{-6}
$\text{Li}_{3.75}\text{Ge}_{0.75}\text{P}_{0.25}\text{O}_4$	-	1 : 0	6.3×10^{-7}
$\text{Li}_{3.75}\text{Ge}_{0.75}\text{P}_{0.25}\text{O}_4$	LiBO_2	1 : 1	1.0×10^{-7}
$\text{Li}_{3.75}\text{Ge}_{0.75}\text{P}_{0.25}\text{O}_4$	B_2O_3	2 : 1	1.4×10^{-8}
$\text{Li}_{6.6}\text{La}_3\text{Zr}_{1.6}\text{Ta}_{0.4}\text{O}_{12}$	Li_3BO_3	1 : 3	unmeasurable
$\text{Li}_{0.33}\text{La}_{0.56}\text{TiO}_3$	Li_3BO_3	1 : 1	unmeasurable
Al-doped $\text{LiTi}_2(\text{PO}_4)_3$	Li_3BO_3	1 : 3	3.2×10^{-8}
$\text{Li}_{3.75}\text{Ge}_{0.75}\text{P}_{0.25}\text{O}_4$	Li_2CO_3	1 : 1	9.5×10^{-7}
$\text{Li}_{3.75}\text{Ge}_{0.75}\text{P}_{0.25}\text{O}_4$	$\text{Li}_{2.2}\text{C}_{0.8}\text{B}_{0.2}\text{O}_3$	1 : 1	9.3×10^{-7}
$\text{Li}_{3.75}\text{Ge}_{0.75}\text{P}_{0.25}\text{O}_4$	LiNO_3	1 : 1	1.8×10^{-7}

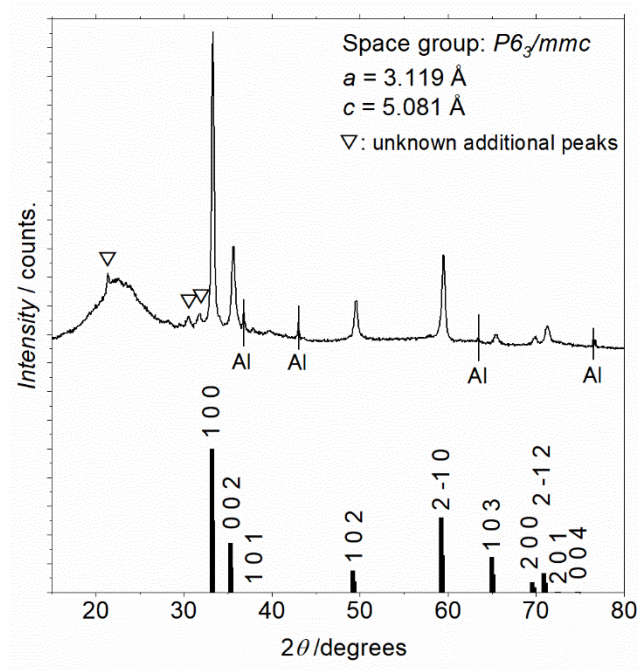


Figure S5. Powder XRD patterns of amorphous 0.5LGPO-0.5Li₃BO₃ after heat treatment at 400 °C and simulated pattern of hexagonal structure (space group: $P6_3/mmc$).

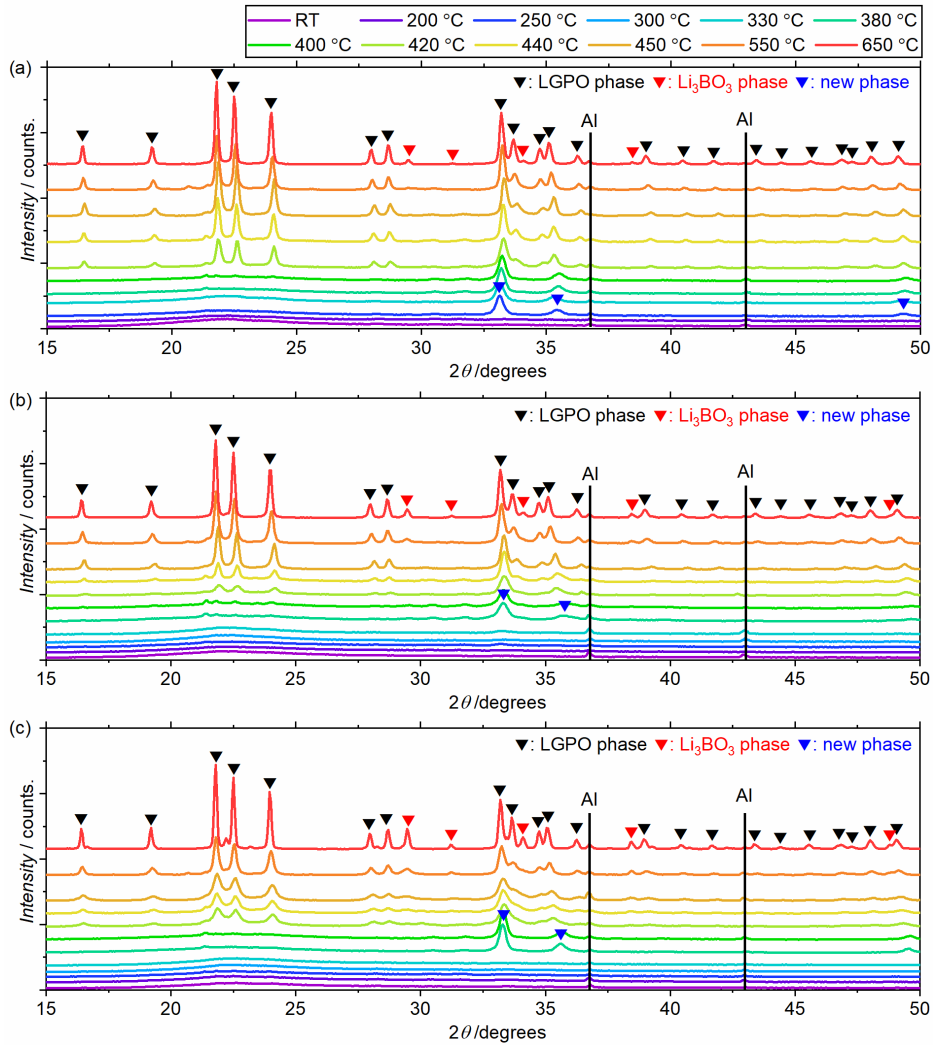


Figure S6. XRD patterns of (a) 0.8LGPO-0.2Li₃BO₃, (b) 0.67LGPO-0.33Li₃BO₃, and (c) 0.5LGPO-0.5Li₃BO₃ amorphous compacts after heat treatment at various temperatures.

Ionic conductivities and microstructures after heat treatment

Figure S7 shows Arrhenius plots for the ionic conductivities of the uniaxially pressed $(1-x)\text{LGPO}-x\text{Li}_3\text{BO}_3$ amorphous compacts ($x = 0.2, 0.33, 0.5$) and of pure LGPO sintered by SPS at various operating temperatures. As discussed above, the conductivity of the 700-°C-heated $(1-x)\text{LGPO}-x\text{Li}_3\text{BO}_3$ compact was close to but slightly less than that of the pure LGPO sintered compact at each temperature since mixing of the low-conductivity Li_3BO_3 additive reduces the total conductivity. However, the activation energy for ionic conduction of $(1-x)\text{LGPO}-x\text{Li}_3\text{BO}_3$, $E_a = 0.48$ eV, estimated from the slope of the Arrhenius plots did not change with the Li_3BO_3 additive ratio and was similar to that of the pure LGPO sintered compact ($E_a = 0.47$ eV), as summarized in Table S3. To investigate this observation, the microstructure of the 700-°C-heated $(1-x)\text{LGPO}-x\text{Li}_3\text{BO}_3$ compacts was observed. As illustrated in Figure S8(a-c), the LGPO crystalline grains (light-gray) and Li_3BO_3 crystalline grains (dark-gray or black) nucleated separately, which agrees with the XRD results [Figure S6(a-c)]. Additionally, the SEM-EDX mappings of Ge in Figure S8(d-f) confirm the distribution of LGPO crystalline grains (green) in the compacts. For samples with less Li_3BO_3 additive ($x = 0.2$ or 0.33), the compact was mostly formed by connected LGPO crystalline grains, and the Li_3BO_3 crystalline grains (or pores) filled in the gaps. The LGPO-connected paths became thin with an increased amount of Li_3BO_3 additive ($x = 0.5$) in the compact but were still connected and associated with the formation of an LGPO mesh network. Therefore, the increase in low-conductivity Li_3BO_3 additive resulted in a decrease in the pre-exponential factor but did not affect the activation energy E_a .

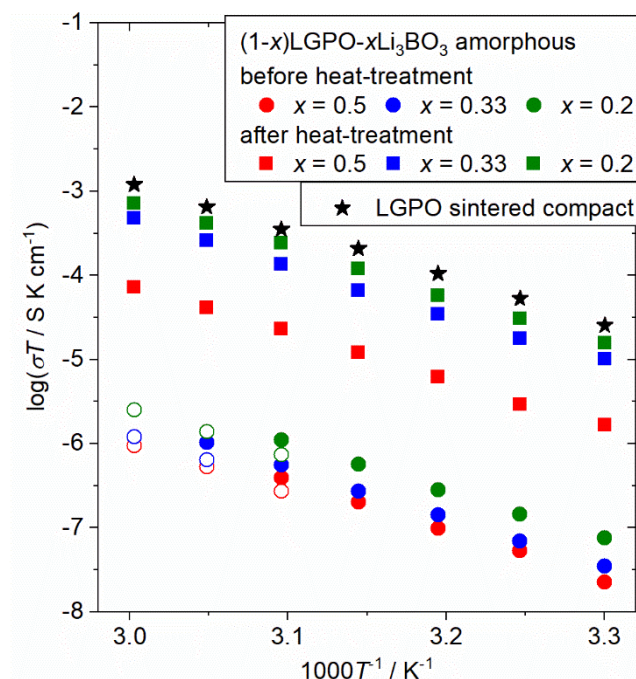


Figure S7. Arrhenius plots of ionic conductivities estimated from Nyquist plots of Au/uniaxially pressed (1-x)LGPO-xLi₃BO₃ amorphous pellet/Au ($x = 0.2, 0.33, 0.5$) at various operating temperatures before heat treatment (circles) and after 700-°C heat treatment (squares). Those of Au/pure LGPO sintered pellet/Au are also shown (stars).

Table S3. Activation energies E_a for ionic conduction of LGPO and (1-x)LGPO-xLi₃BO₃ estimated from the slope of the Arrhenius plots

	Activation energy E_a / eV
Li _{3.75} Ge _{0.75} P _{0.25} O ₄ (LGPO) compact sintered by SPS at 800 °C	0.47
Amorphous 0.8LGPO-0.2Li ₃ BO ₃ before heat treatment	0.51
Amorphous 0.67LGPO-0.33Li ₃ BO ₃ before heat treatment	0.49
Amorphous 0.5LGPO-0.5Li ₃ BO ₃ before heat treatment	0.50
Amorphous 0.8LGPO-0.2Li ₃ BO ₃ after 700-°C heat treatment	0.48
Amorphous 0.67LGPO-0.33Li ₃ BO ₃ after 700-°C heat treatment	0.48
Amorphous 0.5LGPO-0.5Li ₃ BO ₃ after 700-°C heat treatment	0.48

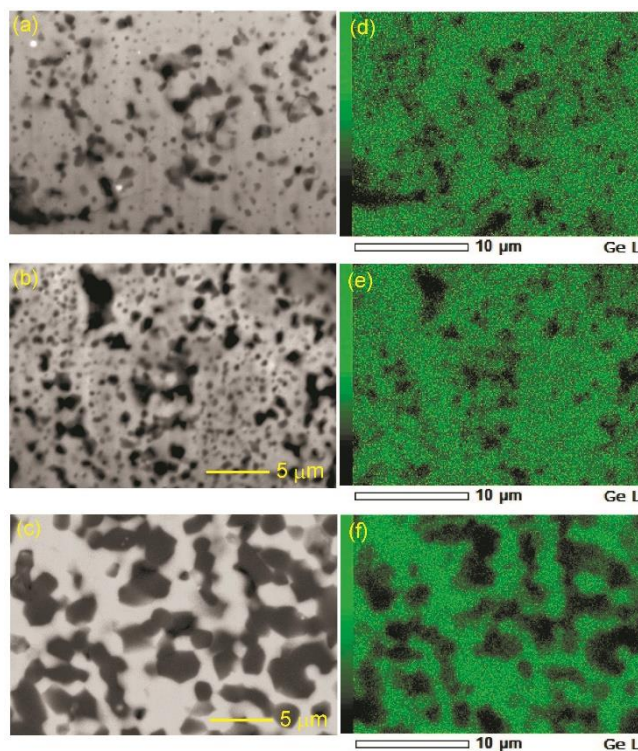


Figure S8. Cross-sectional SEM images of $(1-x)\text{LGPO}-x\text{Li}_3\text{BO}_3$ amorphous compacts [(a) $x = 0.2$, (b) $x = 0.33$, and (c) $x = 0.5$] after 700-°C heat treatment. SEM-EDX mappings of Ge [(d) $x = 0.2$, (e) $x = 0.33$, and (f) $x = 0.5$].

Table S4. Ionic conductivities of 0.5LGPO-0.5Li₃BO₃ amorphous compacts operated at 25 °C before and after heat treatment under various conditions.

0.5LGPO-0.5Li ₃ BO ₃ amorphous electrolyte	Conductivities at 25 °C / S cm ⁻¹
Only pressing at 800 MPa	1.5×10^{-6}
Heating uniaxial compact at 700 °C for 2 h in a conventional furnace	1.1×10^{-5}
Heating at 300 °C for 1 min with a pressure of 400 MPa by SPS	5.0×10^{-6}
Heating at 400 °C for 1 min with a pressure of 400 MPa by SPS	6.3×10^{-6}
Heating at 500 °C for 1 min with a pressure of 400 MPa by SPS	9.5×10^{-7}

Table S5. Reflection planes of amorphous 0.5LGPO-0.5Li₃BO₃ after SPS heat treatment at 400 °C corresponding to selected diffraction spots in Figure 5(d).

Spot number	d^* / nm ⁻¹	Reflection plane candidate of Li _{3.75} Ge _{0.75} P _{0.25} O ₄
ring-a	2.55	2 1 0 or 0 1 1
ring-b	3.71	2 2 0, 4 0 0, or 3 1 1
ring-c	6.42	6 2 0 or 0 4 0
#1	3.91	2 0 0
#2	3.96	2 0 0
#3	3.96	2 0 0
#4	5.31	4 0 2 or 2 2 2
#5	5.37	4 0 2 or 2 2 2

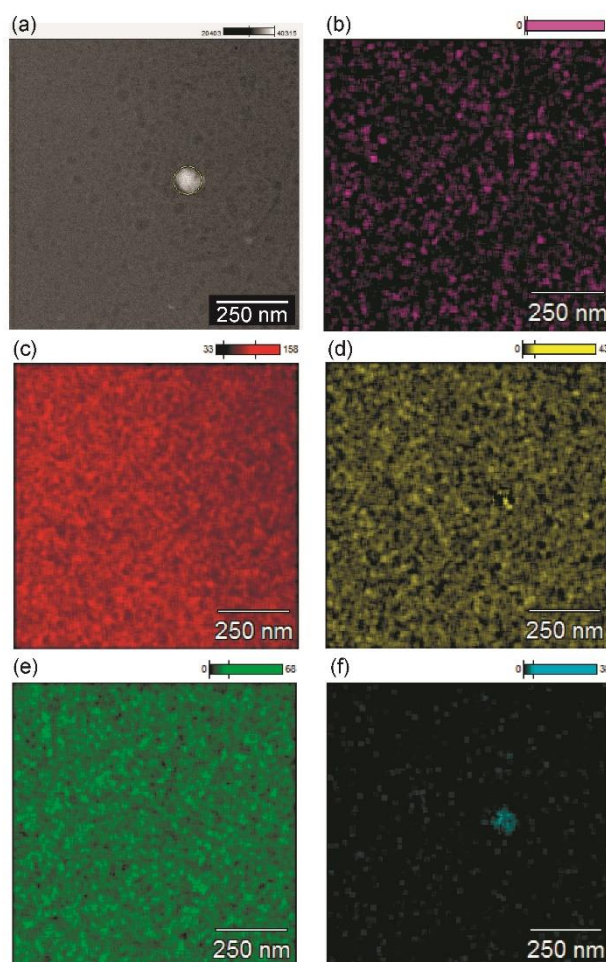


Figure S9. STEM-EDS results of 400-°C-SPS 0.5LGPO-0.5Li₃BO₃ compact; (a) STEM image and STEM-EDS mappings of (b) B, (c) O, (d) P, (e) Ge, and (f) Zr.

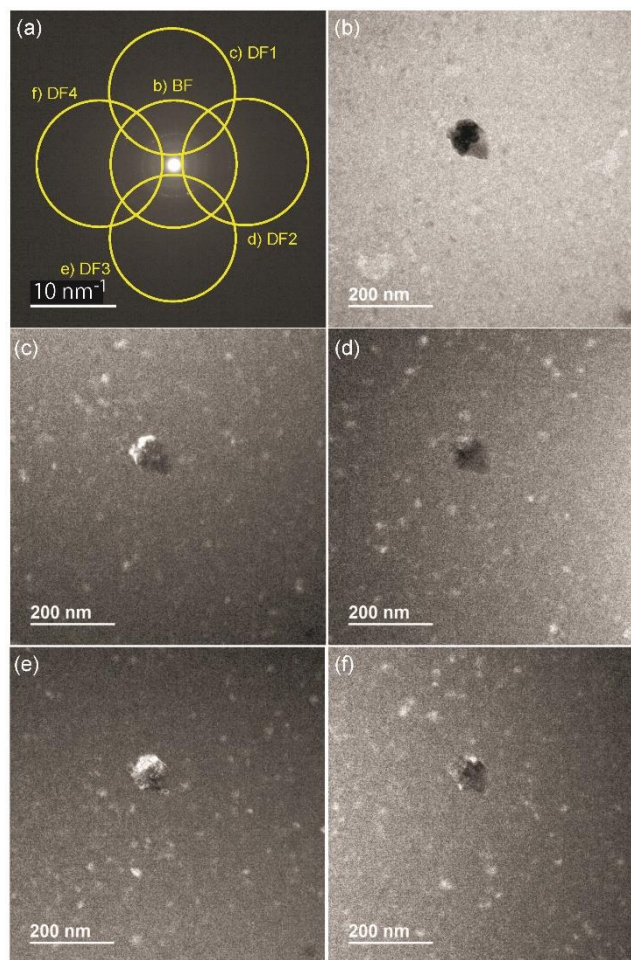


Figure S10. (a) Objective aperture locations for bright-field and dark-field TEM (yellow circles) in electron diffraction of 400-°C-SPS 0.5LGPO-0.5Li₃BO₃ compact. (b) Bright-field TEM image taken with the aperture indicated as circle in (a). (c-f) Dark-field TEM images taken with the aperture location shown in (a). The large grain is ZrO₂ contamination.